THE JOURNAL OF PHYSICAL CHEMISTRY LETTERS
A JOURNAL OF THE AMERICAN CHEMICAL SOCIETY

pubs.acs.org/JPCL

Letter

Spectroscopic Signature of Metal-hydroxo and Peroxo Species in K-edge X-ray Absorption Spectra

Olga Maximova, Roman Ezhov, Scott Jensen, Chengjun Sun, and Yulia Pushkar*

Cite This: *J. Phys. Chem. Lett.* 2024, 15, 11077−11086

Read Online

ACCESS | Metrics & More | Article Recommendations | Supporting Information

ABSTRACT: Metal-dioxygen species are important intermediates formed during dioxygen activations by metalloenzymes in various biological processes, by catalysts in fuel cells, and prior to O_2 evolution by photosystem II. In this work, we focus on manganese-porphyrin complexes using tetramesitylporphyrin ligand (TMP) to explore changes in Mn K-edge X-ray absorption spectroscopy (XAS) associated with the formation of Mn-hydroxide and Mn−O_2 peroxide species. With limited spectroscopic characterization of these compounds, Mn K_β X-ray emission spectroscopy (XES), XAS, density functional theory (DFT), and time-dependent DFT (TD-DFT) analysis will enhance our understanding of their complex electronic structure. We show that the shape of the pre-edge in the K-edge Mn X-ray absorption near-edge structure (XANES) can serve as a spectroscopic signature of the Mn^{III}-peroxo formation and thus can be used to track the presence of the side-on peroxide as an intermediate in time-resolved or *in situ* experiments. Our results will help to further summarize the spectroscopic fingerprints for peroxo and hydroxo species, addressing the challenge of identifying the reactive metal species in catalytic reactions.

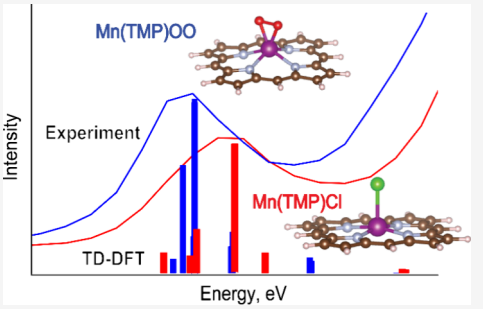

Metalloenzymes activate dioxygen for a variety of biological processes.[1] Dioxygen activation is also important in the development of fuel cells for green energy applications. The general understanding of this process involves dioxygen binding to a reduced metal, formation of superoxo and peroxo intermediates, followed by O−O bond cleavage leading to high-valent metal-oxo species that perform substrate oxidations or result in water formation as the final reduced product in the fuel cell.[1] A similar path but in reverse is followed by the Mn_4Ca cluster of oxygen-evolving complex (OEC) of photosystem II (PS II) during water oxidation and O_2 formation,[2,3] as well as by catalysts facilitating water oxidation reaction. In the process of water oxidation, the high-valent metal-oxo species can couple together via the radical coupling mechanism to produce peroxo species or metal-oxo species can activate water to form peroxide in a process of water nucleophilic attack.[4]

Despite its far-reaching consequences for both fundamental biophysics and applied oxidation catalysis and clean energy research, spectroscopic analysis of reaction mechanisms with peroxo species is very challenging due to their short lifetimes and the mostly transient nature of peroxo species during reactions. Thus, much progress in understanding the structural and chemical properties of peroxo intermediates has been demonstrated while studying biomimetic model compounds.[5−12] Several ligand scaffolds can support stable Mn^{III}−O_2 moieties where the O_2^{2-} group is a side-on peroxide.[13−21] A number of peroxomanganese complexes have been characterized by XRD, EPR, vibrational and X-ray spectroscopy, and computational studies.[13−34] The structural, electronic, and chemical properties of some of them were summarized in review by Leto et al., 2014.[35] XRD measurements of such structures have shown an O−O bond distance of ∼1.4 Å,[13,18] while in all these reports Mn^{III} was coordinated to four nitrogens of the ligand in tetragonal pyramid form. X-ray spectroscopy provides the most direct way to probe the electronic structure and geometry of the first coordination, although there are only a few reports on Mn K-edge XAS (see Table S1). The identification of spectroscopic signatures of metal-peroxo and superoxo species is difficult, and no systematic studies are currently available. At the same time such studies would be helpful to identify the electronic structure of reactive intermediates in the Kok cycle of the OEC monitored by time-resolved XAS.

Here we use manganese-porphyrin complexes (Scheme 1) with a tetramesitylporphyrin ligand (TMP) to explore the changes in Mn K-edge XAS spectra associated with the formation of the Mn-hydroxide and Mn−O_2 peroxide species. While the limited spectroscopic characterization for compounds in Scheme 1 has been reported,[15,36] the XAS, DFT, and TD-DFT analysis will contribute to the understanding of the complex electronic structure and provide insight into the

Received: July 11, 2024
Revised: October 2, 2024
Accepted: October 10, 2024

https://doi.org/10.1021/acs.jpclett.4c02020
J. Phys. Chem. Lett. 2024, 15, 11077−11086

Scheme 1. Mn^{III}-Tetramesitylporphyrin (TMP) Complexes and Their Chemical Transformations

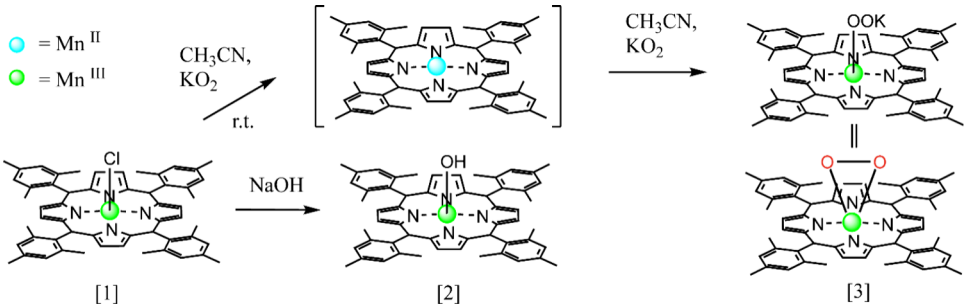

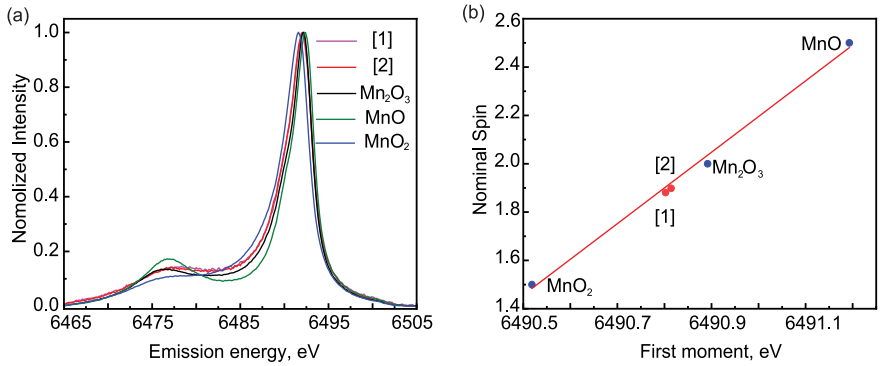

Figure 1. Mn K_β XES spectra of [1, 2] and reference compounds (MnO, Mn_2O_3, and MnO_4) (a) and first moment analysis (b).

Scheme 2. d-Orbitals Splitting in Tetragonal Pyramidal Crystal Field (a) and Schematic Spin Distribution for High Spin (HS) Mn^{III} (b)

nature of the characteristic pre-edge transitions of these complexes at the Mn K-edge. The Mn K_β XES data support the identification of the spin and charge states of Mn ions in compounds [1, 2]. We further expand the experimental XANES data and XANES modeling effort for compounds with different ligand scaffolds to assess the effect of ligand symmetry, the type of ligating atoms, and features of side-on O_2^{2-} versus protonated −OOH.

X-ray Emission Spectroscopy (XES) Characterization. Mn K-edge XES is sensitive to the oxidation state and nominal spin.[37−40] The Mn K_β XES originates from 3p to 1s electron transitions after a 1s core hole is created by an incident X-ray beam. The exchange interaction between the 3p hole in the final state and the Mn 3d electrons manifests in the XES spectra as the $K_{\beta'}$ and $K_{\beta1,3}$ features corresponding to antiparallel and parallel coupling, respectively. The position of the lines and their energy splitting are sensitive to the oxidation state and spin state of Mn.[37,41−43] Due to the 3p nature of K_β XES, it is a more sensitive probe of the oxidation state of the studied element than XANES which is affected by the ligand environment. The K_β XES spectra of [1] and [2] are shown in Figure 1a in comparison to the reference compounds (MnO, Mn_2O_3, and MnO_2).

The positions of spectral lines for [1, 2] are close to the Mn_2O_3 spectrum, which is indicative of Mn^{3+} in a high spin state (HS), $S = 2$. The first moment analysis is commonly used to determine the nominal spin of the studied ion. The first moment is calculated as FM = $\sum_i E_i I_i / \sum_i I_i$, where E_i is the emission energy and I_i is the intensity of the spectrum at that energy. A first moment analysis of all samples was done over the 6485−6495 eV range, which covers the $K_{\beta1,3}$ spectral feature. A linear relationship between the first moment value and nominal spin is determined by carrying out a linear least-squares fit to Mn oxide data.[38] The resulting linear fits describe the nominal spin well with $R^2 = 0.99$. The nominal spin of [1, 2] is ∼1.9, which agrees with a high spin (HS) $S = 2$ electron configuration for d-orbital splitting in a trigonal pyramid crystal field (see Scheme 2). The K_β lines in XES spectra are determined by the (3p, 3d) exchange interaction, making them sensitive to the electron density localized on the metal ion. Compounds [1, 2] have different ligands and geometries in the first coordination sphere of the Mn ion compared to the reference compounds, leading to differences in spin density distribution between the metal ion and its ligands, referred to as covalency. In the measured spectrum, this covalency is reflected in differences in the absolute values of the first

https://doi.org/10.1021/acs.jpclett.4c02020
J. Phys. Chem. Lett. 2024, 15, 11077−11086

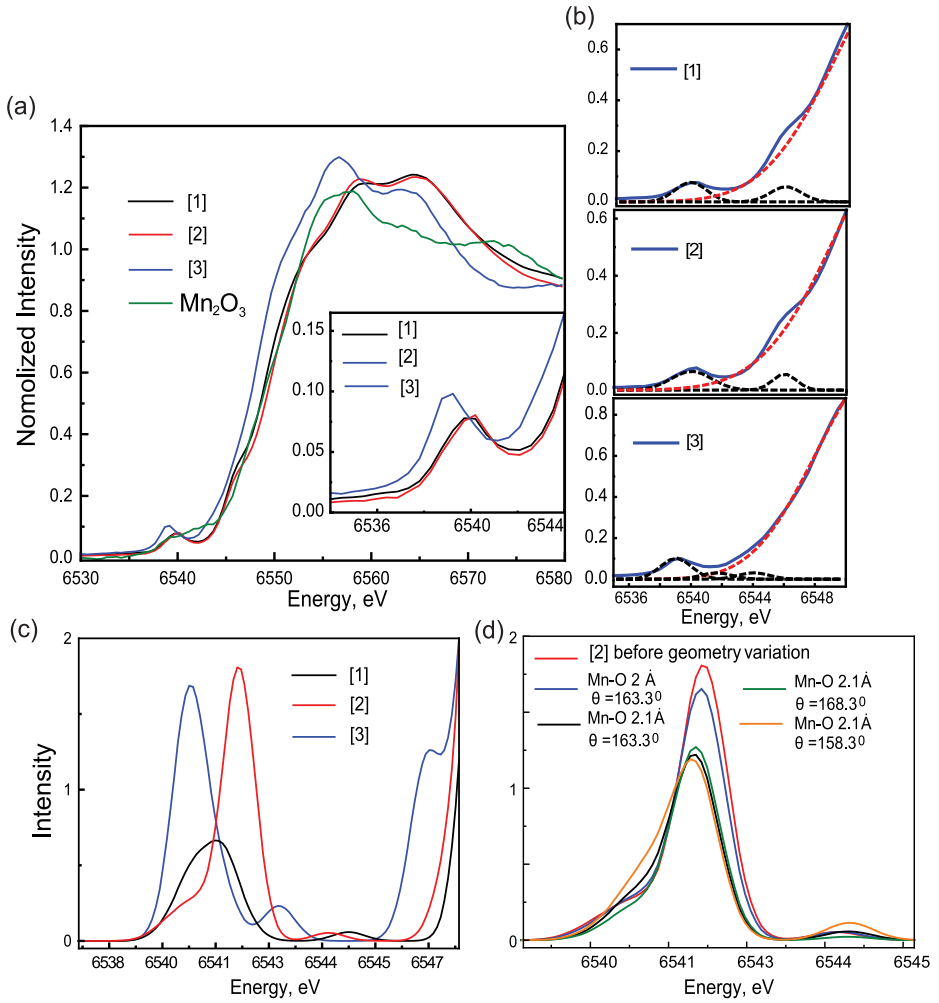

Figure 2. Mn K-edge XANES of [1]−[3] and Mn_2O_3 (a), fitting of the pre-edge region with three Gaussian peaks and the rising edge background for [1]−[3] (b), TD-DFT calculated pre-edge regions for geometry of [1]−[3] derived from DFT energy minimization (c), and for [2] showing the effect of Mn−O bond distance and angle on the pre-edge spectrum (d). The calculated spectra were shifted by 32.6 and 1 eV Gaussian broadening was applied to electronic transitions. The schematic representation of angle θ is shown in Table 3.

moments and the lower nominal spin values relative to Mn_2O_3, as shown by the linear relation in Figure 1a. DFT calculations for [1, 2] show indistinguishable Mulliken spin values on the Mn ions of ρ_{Mn} = 4.02 (2.01) and ρ_{Mn} = 3.94 (1.97) correspondingly. This is in good agreement with the experimental XES data, showing no differences in the position of the K_β line for the two compounds. The absolute value of spin density predicted by DFT and measured in the experiment differ by less than ∼0.1, which we consider to be within the uncertainty of the DFT method. DFT also correctly predicts the high spin state by showing S = 2 to be the lowest-energy state (Table S2).

XAS Characterization. The normalized Mn K-edge XAS of [1]−[3] is shown in Figure 2a. The XANES contains a pre-edge feature at 6540.4 eV and the rising edge with a shoulder at 6547 eV assigned to metal-to-ligand charge transfer (MLCT) transition.[44,45] The latter is in agreement with the significant metal-porphyrin bonding in these compounds.[36,46] The inset shows the magnified pre-edge part of the spectra originating from an electric dipole-forbidden quadrupole-allowed 1s → 3d transition which can gain intensity through 4p mixing into the 3d orbitals if the molecule deviates from centrosymmetry.[41] In general terms, the energy position of the pre-edge transition depends on the crystal field at the absorbing center and its oxidation state. The pre-edge peak for [3] is shifted to lower energies compared to [1]−[2], which might indicate a decrease in crystal field strength or a decrease in the Mn ion oxidation state. The total area of the pre-edge peak for [3] is 1.3 times larger compared to [1] (see Table 1), which is comparable to that previously observed for the Mn^{III}-peroxo complexes.[26,31]

The Mn K-edge energy position corresponds to the *1s* → *4p* transitions and shifts to higher energies with an increase in the metal oxidation state. The comparison of XANES spectra of

Table 1. Experimental and Calculated Pre-edge IWAE (eV), Heights, and Areas[a]

	Calculations			Experiment		
	Predicted area[b]	IWAE, eV	Intensity[b]	Area[b]	IWAE, eV	Intensity[b]
[1]	1	6541.1	1	1	6539.9	1
[2]	2.17	6541.7	2.71	1.01	6539.9	1
[3]	2.19	6540.7	2.72	1.34	6539.2	1.25

[a]For [3] the results for Q = −1 and S = 2 configuration are presented. [b]Shown relative to [1] where [1] is assigned value 1.

https://doi.org/10.1021/acs.jpclett.4c02020
J. Phys. Chem. Lett. 2024, 15, 11077−11086

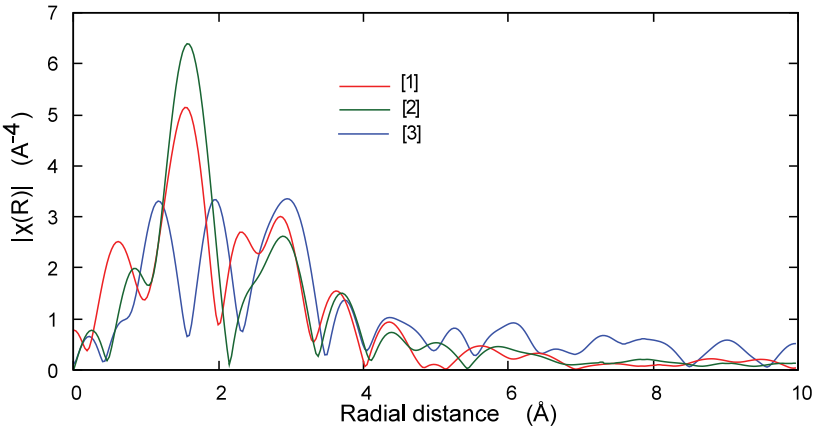

Figure 3. Mn K-edge EXAFS data for [1]−[3].

Table 2. Comparison of Mn-Ligand Bond Distances from EXAFS Fits[a] and DFT

		EXAFS					DFT[c]
Sample	Shell	*R*, Å	*N*[b]	$\sigma^2 \times 10^3$	*R*-factor	Reduced Chi^2	*R*, Å
Mn^{III}(Cl)(TMP) [**1**]	Mn−N	2.09	4	3.6	0.07	2959	2.03
	Mn−Cl	2.48	1	0.7			2.42
	Mn−C	3.17	8	5.9[b]			3.07
	Mn−C	3.39	4	5.9[b]			3.45
	Mn−C	4.32	8	5.9[b]			4.29
Mn^{III}(OH)(TMP) [**2**]	Mn−O	1.90	1	0.6	0.06	3089	1.97
	Mn−N	2.06	4	2.2			2.04
	Mn−C	3.11	8	7.0[b]			3.07
	Mn−C	3.43	4	7.0[b]			3.45
	Mn−C	4.13	8	7.0[b]			4.30
[**3**]	Mn−O	1.86	2	1.3	0.06	767	1.88
	Mn−N	2.15	4	5.1			2.19
	Mn−C	3.24	8	4.8[b]			3.21
	Mn−C	3.56	4	4.8[b]			3.54
	Mn−C	4.25	8	12.0			4.44

[a]Fits were done in *q*-space. *R* is the Mn−backscatter distance. σ^2 is Debye−Waller factor. *R*-factor and Reduced Chi^2 are the goodness-of-fit parameters (see SI, XAS/EXAFS Section). $S_o^2 = 1.0$ was used in all fits. [b]Denotes when σ^2−was set to be the same for vectors in the first (and/or second) coordination shells. [c]Only averaged distances are given. For information on individual Mn-backscatter distances in the first coordination sphere see Table 3.

[1]−[3] and the Mn_2O_3 reference compound measured as a pellet in transmission is shown in Figure 2a. The rising-edge positions of [1]−[2] almost coincide with that for Mn_2O_3, indicating, in agreement with XES, that manganese ions are predominantly in the Mn^{III} oxidation state.

Both the pre-edge and rising edge can be fitted with Gaussian curves, as shown in Figure 2b. Spectra of [1]−[2] can be best described by two features: a lower-intensity peak at 6540 eV and higher-intensity peaks at 6546 eV, assigned earlier to MLCT. For comparison, the alternative fittings for [1]−[2] with three peaks are given in Figure S2. For [3] the same range was fitted with three components at 6539, 6542, and 6544 eV (Figure 2b). [1] and [2] demonstrate pronounced MLCT at around 6546 eV, and we can speculate that its intensity decreases and shifts to lower energies in [3]. In ref 44 it was shown that ligands of primarily π-acceptor character cause intense absorptions at the rising edge, which appear as clearly visible shoulders on the edge. Based on these previous observations, the current experimental spectra can indicate a significant quadrupole transition moment due to charge transfer to the porphyrin ring, resulting in an intense MLCT peak in [1]−[2].

The Extended X-ray Absorption Fine Structure (EXAFS) was used to investigate the local geometry of [1]−[3] (Figure 3). The EXAFS data, non-phase-shift corrected Fourier transform, and best fits are shown in Figure S1. The structural parameters obtained from the EXAFS fits for [1]−[3] are summarized in Table 2 and Table S3.

The EXAFS data for [1]−[2] point to a five-coordinated Mn center. The bond lengths derived from DFT computations for [1]−[2] are in good agreement with the parameters obtained from EXAFS fitting (Table 2). The slightly different Mn−N bond lengths in the first coordination sphere, as predicted by DFT (2.17 and 2.22 Å, Table 3), result in an increased Debye−Waller (DW) factor when fitting the EXAFS data with a single Mn−N shell model (Table 2). This reflects the variation in the average backscatter distance due to the presence of two distinct Mn−N distances. The DFT-optimized structure of [1] features a Mn−Cl distance of 2.42 Å, slightly shorter than the EXAFS-determined distance of 2.48 Å. The computed 1.97 Å Mn−OH bond length in [2] is consistent with the EXAFS-determined distance (1.90 Å). In the DFT optimized structure, the N−Mn−N angles across the ligand are

https://doi.org/10.1021/acs.jpclett.4c02020
J. Phys. Chem. Lett. 2024, 15, 11077−11086

Table 3. DFT-Calculated Energy Values and Structural Parameters for [1]−[3]

	Calculations parameters Q-charge S- spin	Mn electronic configuration	Gibbs free energy, eV	Structural parameters	Mn atomic spin population
[1] 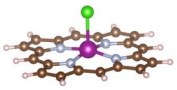	Q=0, S=2	Mn(III,S=2)	-70753.74	Mn-Cl: 2.42 Å Mn-N: 2.03 Å Mn-N: 2.03 Å Mn-N: 2.03 Å Mn-N: 2.03 Å <θ=165^0	4.02
[2] 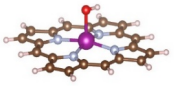	Q=0, S=2	Mn(III,S=2)	-60292.35	Mn-O: 1.97 Å O-H: 0.97 Å Mn-N: 2.03 Å Mn-N: 2.04 Å Mn-C: 3.07 Å Mn-C: 3.45 Å Mn-C: 4.29 Å < θ_1=163.3^0 < θ_2=165.1^0	3.94
[3] 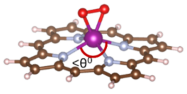	Q=-1, S=2	Mn(III, S=2) S (O_2^{2-}) = 0	-62325.38	Mn-O: 1.88 Å Mn-O: 1.88 Å O-O: 1.43 Å Mn-N: 2.21 Å Mn-N: 2.17 Å Mn-N: 2.21 Å Mn-N: 2.17 Å Mn-C: 3.19 Å Mn-C: 3.39 Å Mn-C: 4.44 Å < θ_1=135.9^0 < θ_2=141.7^0	3.23

S (O_2^{2-}) – spin population of O_2^{2-} ligand

about ∼164° (Table 3), indicating that the Mn ion is slightly out of the ligand plane (see Scheme 2b).

The best fit for [3] indicates a six-coordinated geometry, composed of two Mn−O at 1.86 Å, four Mn−N at 2.15 Å, and three Mn−C shells at distances of 3.24−4.25 Å which are similar to [1]−[2] structures (Table 2). The observed Mn−O and Mn−N values are comparable to bond distances obtained from EXAFS data for Mn^{III} high spin peroxo complexes[26,31] and in XRD of a similar $Mn^{III}TPPO_2$ complex.[13]

Compound [3] received limited spectroscopic characterization earlier, and its exact electronic structure is not firmly established. UV−vis spectra of [3] in acetonitrile used as a solvent in XAS experiments is similar to the spectra in dichloromethane (Figure S5).[15] The dichloromethane solvent was not suitable for XAS experiments due to high X-ray absorption. [3] can be chemically viewed as a result of a ligand exchange on the Mn^{III} ion from Cl^- to O_2^-, and if so, a neutral complex $[(TMP)MnO_2]^0$ should form. However, the superoxide ligand is redox active and the original report noted a possible evolution of oxygen in the reaction.[15] Reduction by one electron would produce $[(TMP)MnO_2]^-$ which most likely has a charge distribution as a Mn^{III} peroxo (O_2^{2-}) complex.

$$[(TMP)Mn^{III}O_2]^0 + O_2^- = [(TMP)Mn^{III}O_2]^- + O_2 \quad (1)$$

We further used DFT calculations with the same approach as for [1]−[2] where DFT correctly predicted the HS state (S = 2) of the Mn^{III} center and the geometry of the complex (see Table S2) to assess both possible states of the complex [3]. Table S4 summarizes the energy after geometry optimization for [3] computed in several electronic configurations of the Mn ion in accordance with the total charge and spin of the complex, assuming an end-on and side-on O−O initial structure. Specifically, it can be seen from the energy diagram at Scheme 2a that for an electrically neutral complex (charge Q = 0) and negatively charged complex (charge Q = −1) there are three possible and four possible values of a total spin, correspondingly (see column 1 of Table S4). The DFT-derived electron configurations of the Mn ion and dioxygen species are indicated with bold font in Table S4. The DFT-predicted values for Mn−O, Mn−N, and Mn−C distances for lowest-energy configuration (Table 3) agree well with the ones obtained from EXAFS. The calculated Mn−O and O−O bond lengths fall within a range of 1.84−1.90 Å and 1.40−1.43 Å for Mn^{III}-peroxo complexes, as determined from crystallographic and spectroscopic characterization.[13,16−18,20,21,26,31,35] According to DFT calculations, [3] forms the $Mn^{III}O_2$ side-on peroxo species (S = 2) (see Table S4). The DFT derived values for Gibbs energies enable us to estimate the change in free energies for reaction (1) to be about −0.3 eV (Table S5), which suggests that reaction (1) is plausible from an energetic standpoint.

According to DFT calculations, the most favorable structure for [3] corresponds to the Mn ion in tetragonal pyramidal coordination (Scheme 2). The Mn ion is located further out of the plane of equatorial ligand in [3] compared with [1] and [2] as indicated by the N−Mn−N angles in DFT-optimized structures (Table 3). The observed changes in geometry affect the crystal field splitting of Mn d orbitals and the intensity of the 1s−3d pre-edge transitions (see Scheme 2) which result in the spectral differences observed in XANES spectra for [1]−[3].[47,48]

https://doi.org/10.1021/acs.jpclett.4c02020
J. Phys. Chem. Lett. 2024, 15, 11077−11086

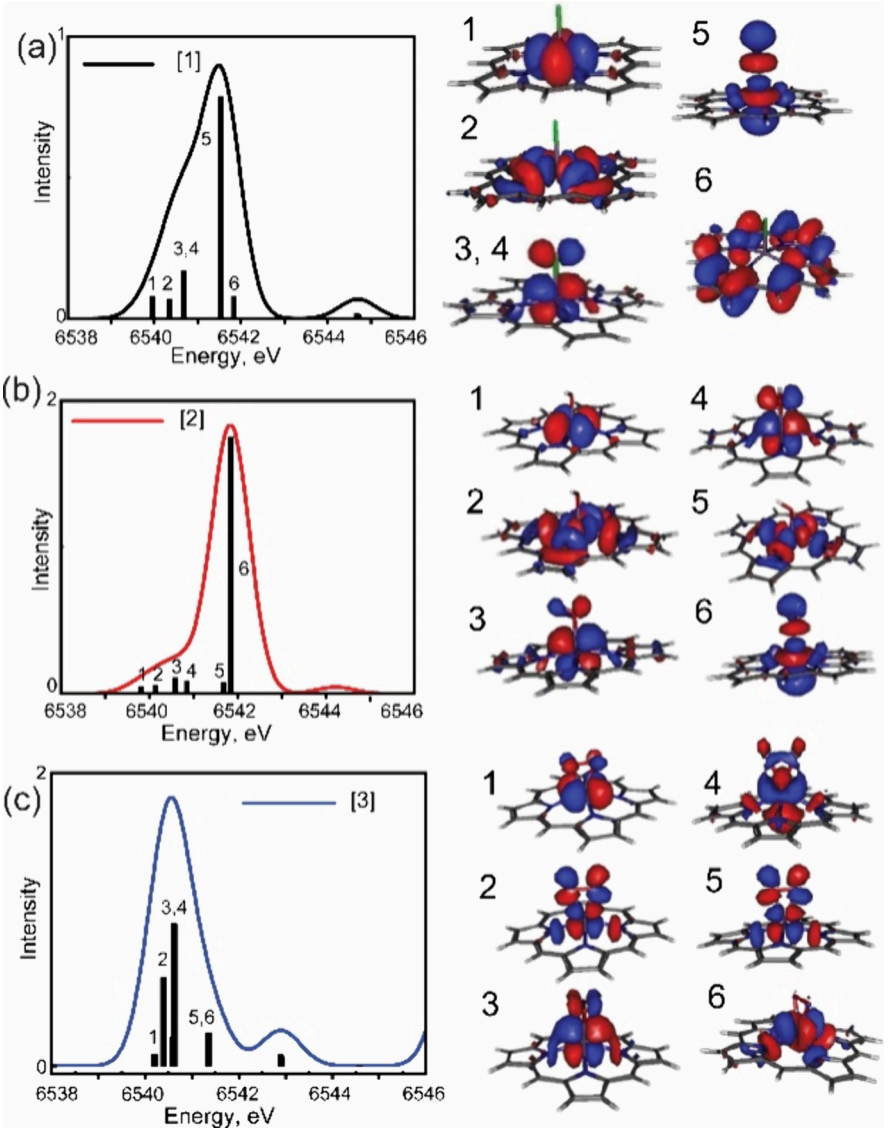

Figure 4. Calculated pre-edge regions and corresponding NTO for [1] (a), [2] (b), and [3] (c). For [3], the NTO for $Q = -1$ and $m = 5$ configuration is presented.

A detailed correlation between the electronic structure and spectroscopic response requires quantum mechanical calculations. The TD-DFT calculated pre-edge spectra were obtained using the previously described protocol (i.e., density functional, basis set, etc.).[44] The accuracy of the method was quantified in previous studies on mononuclear Mn complexes. The calculated spectra were shifted by 32.6 eV to higher energy to correct for systematic errors in the level of theory.[44] The geometry optimization was performed as described in the section for DFT calculations in the Supporting Information for Mn^{III} in the HS state ($S = 2$) for [1] and [2]. The results of geometry optimization for [3] carried out for side-on and end-on O−O initial geometry and structure parameters are presented in Table S4. The TD-DFT for [3] was performed for the configuration corresponding to overall minimum energy, which is the $Mn^{III}O_2^{2-}$ HS ($S = 2$) state. The results of the TD-DFT of the XANES pre-edge region for [1]−[3] are shown in Figures 2c and 4. The calculated spectra consist of two major features: the lower-energy (∼6539−6541 eV) bands correspond to pre-edge Mn 1s-to-3d transitions, and the bands above 6542 eV arise from MLCT[48] transitions.

Calculations reproduce well the shift in the peak position between [1] and [3] observed in the experiment. Changes in the pre-edge region with ligand modification can be quantified based on the areas of the pre-edge region and the intensity weighted average energies (IWAEs) as shown in Table 1. The area under the pre-edge peak for [3] is larger, and the IWAE is shifted to lower-energy transitions, as was observed in the experiment. The TD-DFT derived pre-edge area was calculated by a previously published method using an empirical equation, $A = 6.01I + 1.79$ for the B3LYP functional, where I is the sum of the electric dipole, electric quadrupole, and magnetic dipole contributions.[44] In the experiment, the intensity of the pre-edge in [1, 2] is ∼1/3 lower in comparison to [3]. However, this trend is not directly reproduced in the TD-DFT spectra of [2]. To explore the factors affecting the intensity of the pre-edge peak in [2] we calculated spectra for changing the Mn−O bond length and the position of the Mn ion relative to the ligand plane (as measured by the N−Mn−N angle). The Mn movement in and out of the plane while keeping the same Mn−O length did not significantly affect the spectra, while the increase of Mn−O distance by 0.2 Å resulted

https://doi.org/10.1021/acs.jpclett.4c02020
J. Phys. Chem. Lett. 2024, 15, 11077−11086

in almost a 2-fold decrease in pre-edge intensity (see Figure 2d). The latter points to the pronounced dependence of the pre-edge intensity on the Mn orbital's overlap with the axial ligand in [2]. The positions of calculated MLCT bands relative to the energy of the pre-edge transitions for [1]−[3] are underestimated when compared to the experiment. However, as a trend, [3] rises prior to [1]−[2] in agreement with the experiment. According to the previous study,[44] the calculated positions of MLCT bands relative to the pre-edge peak in an extended π−ligand system depend on the amount of Hartree−Fock (HF) exchange in the utilized density functional and thus a significant (~3 eV) difference with the experiment can be associated with the functional used for TD-DFT calculations. These effects were not investigated further.

Analysis of the TD-DFT natural transition orbitals (NTOs) for [1]−[3] can help further investigate the nature of the underlying electronic transitions that form the pre-edge region (Figure 4). For [1]−[3], the character of the transitions in each energy region remains essentially the same with the change of the axial ligand. Specifically, the pre-edge region is formed by six transitions from the 1s core orbitals to 3d with dominant local Mn character with some delocalization on ligands meaning some charge transfer to ligands O_2^{2-}, OH^-, Cl^-, and N atoms of TMP. The NTO for state 1 in [1]−[2] has an almost purely 3d character with zero dipole transition moment, and a considerable quadrupole moment giving rise to the intensity of state 1 (see Figure 4), while states 2−6 consist of the Mn 3d orbitals mixing with ligands. This charge transfer on ligands results in a nonzero dipole transition moment, which is canceled out in the porphyrin plane but is not zero for axial ligands. The latter gives rise to the nonzero dipole transition moment for state 5 in [1] and state 6 in [2] corresponding to the most intense peaks in these compounds. In addition, the d-orbital and charge distribution on the ligands give rise to a quadrupole transition moment that contributes to the intensity of pre-edge transitions. The NTOs for [3] indicate the charge transfer for states 1−6 resulting in nonzero dipole transition moment in states 2−4 and 6 that results in the observed differences in the intensity of the pre-edge area.

The previously reported XANES data for the M-O_2 compounds where M = Ni, Fe, Mn indicate that the formation of the peroxo species is often associated with an increased pre-edge intensity.[19,26,31,49,50] The results of TD-DFT calculations presented earlier for Mn−O_2 compounds reproduced the increased pre-edge intensity and were related to a significant (~3−4%) Mn 3d-4p mixing.[26,31] In the case of [3] here, the increase in pre-edge intensity has been mainly associated with the dipole transition moment arising from the charge transfer to ligands. To elucidate which effect is responsible for the increased pre-edge observed in other Mn−O_2 compounds (see Figure S1) we performed TD-DFT calculations for $[Mn^{III}TMC(O_2)]^+$,[19] which has a similar to [1]−[3] ligand geometry. The calculated spectra are presented in Figure S4, and the computed spectrum of $[Mn^{III}TMC(O_2)]^+$ side-on peroxide agrees well with that of [3]. The NTO involved in the transitions indicate the significant charge distribution on the axial ligand in $[Mn^{III}TMC(O_2)]^+$. The initial compound with weakly coordinated $CF_3SO_3^-$ and the state assigned to the protonated end on peroxide had different spectra in agreement with the experiment.[19]

The Mn−O_2 and Fe−O_2 species are relevant in enzymatic oxidation and as intermediates in fuel cells. The mechanism underlying the formation of the O−O bond by the Mn_4Ca cluster in PS II remains debated. A manganese(V)-oxo species has been proposed as an intermediate in the energy-demanding O−O bond formation, which is the most crucial step in dioxygen evolution.[51−54] In 2015, our group proposed a mechanistic model for dioxygen generation by PSII, which assumed the formation of a Mn^{IV}=O fragment prior to the formation of the O−O bond supported by both DFT calculations and XES studies.[55] To decode the processes in PSII, many efforts have been directed to capturing highly reactive Mn-oxo species and products of the O−O bond formation in catalytic water oxidation reactions.[22,56−59] Spectroscopy is the superior approach for understanding the process of O−O bond formation due to the lack of XRD sensitivity to the metal electronic structure and its limited distance resolution for Mn−O bonds in the presence of four heavy Mn ions.[60] Spectroscopy has been efficient at identifying highly oxidized metal-oxo species such as Ru^V=O, Ru^{IV}=O, Fe^V=O, and Co^{IV}=O due to easily detectable short metal-oxo distances in the 1.5−1.7 Å range.[61−64] This study analyzes signatures of the peroxo species in the pre-edge range which, while being low-intensity, is easily accessible.

In summary, we have studied the X-ray spectroscopic properties of a series of tetramesitylmanganese(III) compounds featuring Mn-peroxo and Mn-hydroxo species. The pre-edge XANES for the Mn-peroxo system shows a pronounced pre-edge area compared to the compounds with axial −OH or Cl groups. The TD-DFT study of the compounds presented here, as well as some of the compounds with reported XANES spectra and known crystal structure, indicated a significant contribution of the charge transfer on the ligands resulting in an increased and low-energy shifted pre-edge in Mn-peroxo compounds. Considering that the spectral features at the low energy of the pre-edge area at formation of the M-peroxo species have been observed for a number of other transition metal-based mononuclear compounds,[19,26,31,49,50] we suggest that it can serve as a spectroscopic signature of Mn-peroxo species formation. This result can provide the benchmark for the identification of the Mn^{III}-peroxo intermediates in the reactions of the Mn-based enzymes during time-resolved or *in situ* X-ray absorption experiments.

■ ASSOCIATED CONTENT

Supporting Information

The Supporting Information is available free of charge at https://pubs.acs.org/doi/10.1021/acs.jpclett.4c02020.

Details on material preparations and experimental methods; additional experimental data (Figure S1) and additional calculations results (Tables S1−S5, Figures S2−S5): DFT calculated Mulliken spin population, structural parameters from EXAFS fits, geometry optimization for [3] with side-on and end-on configuration, fitting of the pre-edge region with Gaussian peaks for [1]−[2], calculated pre-edge regions and corresponding NTO for [1]−[3] and $Mn^{II}(TMC)(CF_3SO_3)_2$ (PDF)

■ AUTHOR INFORMATION

Corresponding Author

Yulia Pushkar − *Purdue University, Physics and Astronomy Department, West Lafayette, Indiana 47907, United States;*

https://doi.org/10.1021/acs.jpclett.4c02020
J. Phys. Chem. Lett. 2024, 15, 11077−11086

orcid.org/0000-0001-7949-6472; Email: ypushkar@purdue.edu

Authors

Olga Maximova − *Purdue University, Physics and Astronomy Department, West Lafayette, Indiana 47907, United States;* orcid.org/0000-0001-7789-6683

Roman Ezhov − *Purdue University, Physics and Astronomy Department, West Lafayette, Indiana 47907, United States;* orcid.org/0000-0001-6806-4033

Scott Jensen − *Purdue University, Physics and Astronomy Department, West Lafayette, Indiana 47907, United States;* orcid.org/0000-0002-8446-4800

Chengjun Sun − *Argonne Advanced Photon Source, Argonne National Laboratory, Argonne, Illinois 60439, United States;* orcid.org/0000-0001-9158-8337

Complete contact information is available at: https://pubs.acs.org/10.1021/acs.jpclett.4c02020

Author Contributions

The manuscript was written through contributions of all authors. All authors have given approval to the final version of the manuscript.

Funding

This research was supported by NSF, CHE-2303743 (Y.P.).

Notes

The authors declare no competing financial interest.

■ ACKNOWLEDGMENTS

This research was supported by NSF, CHE-2303743 (Y.P.). This research used resources of the Advanced Photon Source, an Office of Science User Facility operated for the U.S. Department of Energy (DOE) Office of Science by Argonne National Laboratory, and was supported by the U.S. DOE under Contract No. DE-AC02-06CH11357, and the Canadian Light Source and its funding partners. The authors thank Dr. Pavel Pokhilko for helpful discussions.

■ REFERENCES

(1) Nam, W. Dioxygen activation by metalloenzymes and models. *Acc. Chem. Res.* **2007**, *40*, 465−465, DOI: 10.1021/ar700131d.

(2) Kok, B.; Forbush, B.; McGloin, M. Cooperation of charges in photosynthetic O2 evolution−I. A linear four step mechanism. *J. Photochem. Photobiol.* **1970**, *11* (6), 457−475.

(3) Wydrzynski, T. J.; Satoh, K.; Freeman, J. A. *Photosystem II: the light-driven water: plastoquinone oxidoreductase*; Springer, 2005.

(4) Ezhov, R.; Bury, G.; Maximova, O.; Grant, E. D.; Kondo, M.; Masaoka, S.; Pushkar, Y. Pentanuclear iron complex for water oxidation: Spectroscopic analysis of reactive intermediates in solution and catalyst immobilization into the MOF-based photoanode. *J. Catal.* **2024**, *429*, No. 115230.

(5) Solomon, E. I.; Brunold, T. C.; Davis, M. I.; Kemsley, J. N.; Lee, S.-K.; Lehnert, N.; Neese, F.; Skulan, A. J.; Yang, Y.-S.; Zhou, J. Geometric and electronic structure/function correlations in non-heme iron enzymes. *Chem. Rev.* **2000**, *100* (1), 235−350.

(6) Costas, M.; Mehn, M. P.; Jensen, M. P.; Que, L. Dioxygen activation at mononuclear nonheme iron active sites: enzymes, models, and intermediates. *Chem. Rev.* **2004**, *104* (2), 939−986.

(7) Mirica, L. M.; Ottenwaelder, X.; Stack, T. D. P. Structure and spectroscopy of copper−dioxygen complexes. *Chem. Rev.* **2004**, *104* (2), 1013−1046.

(8) Cramer, C. J.; Tolman, W. B. Mononuclear Cu−O2 complexes: geometries, spectroscopic properties, electronic structures, and reactivity. *Acc. Chem. Res.* **2007**, *40* (7), 601−608.

(9) Suzuki, M. Ligand effects on dioxygen activation by copper and nickel complexes: Reactivity and intermediates. *Acc. Chem. Res.* **2007**, *40* (7), 609−617.

(10) Himes, R. A.; Karlin, K. D. Copper−dioxygen complex mediated C−H bond oxygenation: relevance for particulate methane monooxygenase (pMMO). *Curr. Opin Chem. Biol.* **2009**, *13* (1), 119−131.

(11) Yao, S.; Driess, M. Lessons from isolable nickel (I) precursor complexes for small molecule activation. *Acc. Chem. Res.* **2012**, *45* (2), 276−287.

(12) Jensen, S. C.; Davis, K. M.; Sullivan, B.; Hartzler, D. A.; Seidler, G. T.; Casa, D. M.; Kasman, E.; Colmer, H. E.; Massie, A. A.; Jackson, T. A.; et al. X-ray emission spectroscopy of biomimetic Mn coordination complexes. *J. Phys. Chem. Lett.* **2017**, *8* (12), 2584−2589.

(13) VanAtta, R. B.; Strouse, C. E.; Hanson, L. K.; Valentine, J. S. Peroxo (tetraphenylporphinato) manganese (III) and chloro (tetraphenylporphinato) manganese (II) anions. Synthesis, crystal structures, and electronic structures. *J. Am. Chem. Soc.* **1987**, *109* (5), 1425−1434.

(14) Hoffman, B. M.; Weschler, C. J.; Basolo, F. The dioxygen adduct of meso-tetraphenylporphyrinmanganese (II), a synthetic oxygen carrier. *J. Am. Chem. Soc.* **1976**, *98* (18), 5473−5482.

(15) Groves, J. T.; Watanabe, Y.; McMurry, T. J. Oxygen activation by metalloporphyrins. Formation and decomposition of an acylperoxymanganese (III) complex. *J. Am. Chem. Soc.* **1983**, *105* (13), 4489−4490.

(16) Kitajima, N.; Komatsuzaki, H.; Hikichi, S.; Osawa, M.; Moro-oka, Y. A monomeric side-on peroxo manganese (III) complex: Mn (O2)(3, 5-iPr2pzH)(HB (3, 5-iPr2pz) 3). *J. Am. Chem. Soc.* **1994**, *116* (25), 11596−11597.

(17) Singh, U. P.; Sharma, A. K.; Hikichi, S.; Komatsuzaki, H.; Moro-oka, Y.; Akita, M. Hydrogen bonding interaction between imidazolyl N−H group and peroxide: Stabilization of Mn (III)-peroxo complex TpiPr2Mn (η2-O2)(imMeH)(imMeH= 2-methylimidazole). *Inorg. Chim. Acta* **2006**, *359* (13), 4407−4411.

(18) Seo, M. S.; Kim, J. Y.; Annaraj, J.; Kim, Y.; Lee, Y. M.; Kim, S. J.; Kim, J.; Nam, W. [Mn (tmc)(O2)]+: A Side-On Peroxido Manganese (III) Complex Bearing a Non-Heme Ligand. *Angew. Chem.* **2007**, *119* (3), 381−384.

(19) So, H.; Park, Y. J.; Cho, K.-B.; Lee, Y.-M.; Seo, M. S.; Cho, J.; Sarangi, R.; Nam, W. Spectroscopic Characterization and Reactivity Studies of a Mononuclear Nonheme Mn (III)−Hydroperoxo Complex. *J. Am. Chem. Soc.* **2014**, *136* (35), 12229−12232.

(20) Kang, H.; Cho, J.; Cho, K. B.; Nomura, T.; Ogura, T.; Nam, W. Mononuclear Manganese−Peroxo and Bis (μ-oxo) dimanganese Complexes Bearing a Common N-Methylated Macrocyclic Ligand. *Chem. Eur. J. A* **2013**, *19* (42), 14119−14125.

(21) Annaraj, J.; Cho, J.; Lee, Y. M.; Kim, S. Y.; Latifi, R.; De Visser, S. P.; Nam, W. Structural characterization and remarkable axial ligand effect on the nucleophilic reactivity of a nonheme manganese (III)−peroxo complex. *Angew. Chem., Int. Ed.* **2009**, *48* (23), 4150−4153.

(22) Guo, M.; Lee, Y.-M.; Gupta, R.; Seo, M. S.; Ohta, T.; Wang, H.-H.; Liu, H.-Y.; Dhuri, S. N.; Sarangi, R.; Fukuzumi, S.; et al. Dioxygen activation and O−O bond formation reactions by manganese corroles. *J. Am. Chem. Soc.* **2017**, *139* (44), 15858−15867.

(23) Colmer, H. E.; Geiger, R. A.; Leto, D. F.; Wijeratne, G. B.; Day, V. W.; Jackson, T. A. Geometric and electronic structure of a peroxomanganese (iii) complex supported by a scorpionate ligand. *Dalton Trans.* **2014**, *43* (48), 17949−17963.

(24) Gallagher, A. T.; Lee, J. Y.; Kathiresan, V.; Anderson, J. S.; Hoffman, B. M.; Harris, T. D. A structurally-characterized peroxomanganese (IV) porphyrin from reversible O 2 binding within a metal−organic framework. *Chem. Sci.* **2018**, *9* (6), 1596−1603.

(25) Leto, D. F.; Chattopadhyay, S.; Day, V. W.; Jackson, T. A. Reaction landscape of a pentadentate N5-ligated Mn II complex with O 2˙−and H 2 O 2 includes conversion of a peroxomanganese (iii) adduct to a bis (μ-oxo) dimanganese (iii, iv) species. *Dalton Trans.* **2013**, *42* (36), 13014−13025.

(26) Colmer, H. E.; Howcroft, A. W.; Jackson, T. A. Formation, characterization, and O−O bond activation of a peroxomanganese (iii) complex supported by a cross-clamped cyclam ligand. *Inorg. Chem.* **2016**, *55* (5), 2055−2069.
(27) Du, J.; Xu, D.; Zhang, C.; Xia, C.; Wang, Y.; Sun, W. Synthesis, characterization, and reactivity of a side-on manganese (III)−peroxo complex bearing a pentadentate aminopyridine ligand. *Dalton Trans.* **2016**, *45* (25), 10131−10135.
(28) Du, J.; Miao, C.; Xia, C.; Sun, W. A novel manganese (III)-peroxo complex bearing a proline-derived pentadentate amino-benzimidazole ligand. *Chin. Chem. Lett.* **2018**, *29* (12), 1869−1871.
(29) Geiger, R. A.; Chattopadhyay, S.; Day, V. W.; Jackson, T. A. Nucleophilic reactivity of a series of peroxomanganese (III) complexes supported by tetradentate aminopyridyl ligands. *Dalton Trans.* **2011**, *40* (8), 1707−1715.
(30) Geiger, R. A.; Wijeratne, G. B.; Day, V. W.; Jackson, T. A. Steric and electronic influences on the structures of peroxomanganese (III) complexes supported by tetradentate ligands. *Eur. J. Inorg. Chem.* **2012**, *2012* (10), 1598−1608.
(31) Denler, M. C.; Wijeratne, G. B.; Rice, D. B.; Colmer, H. E.; Day, V. W.; Jackson, T. A. Mn III-Peroxo adduct supported by a new tetradentate ligand shows acid-sensitive aldehyde deformylation reactivity. *Dalton Trans.* **2018**, *47* (38), 13442−13458.
(32) Shook, R. L.; Gunderson, W. A.; Greaves, J.; Ziller, J. W.; Hendrich, M. P.; Borovik, A. A monomeric MnIII−peroxo complex derived directly from dioxygen. *J. Am. Chem. Soc.* **2008**, *130* (28), 8888−8889.
(33) Narulkar, D. D.; Ansari, A.; Vardhaman, A. K.; Harmalkar, S. S.; Lingamallu, G.; Dhavale, V. M.; Sankaralingam, M.; Das, S.; Kumar, P.; Dhuri, S. N. A side-on Mn (iii)−peroxo supported by a non-heme pentadentate N 3 Py 2 ligand: synthesis, characterization and reactivity studies. *Dalton Trans.* **2021**, *50* (8), 2824−2831.
(34) Geiger, R. A.; Leto, D. F.; Chattopadhyay, S.; Dorlet, P.; Anxolabéhère-Mallart, E.; Jackson, T. A. Geometric and electronic structures of peroxomanganese (III) complexes supported by pentadentate amino-pyridine and-imidazole ligands. *Dalton Trans.* **2011**, *50* (20), 10190−10203.
(35) Leto, D. F.; Jackson, T. A. Peroxomanganese complexes as an aid to understanding redox-active manganese enzymes. *JBIC* **2014**, *19*, 1−15.
(36) Arasasingham, R. D.; Bruice, T. C. Reaction of hydroxide ion with manganese (III) tetramesitylporphyrin and the oxidation states of manganese tetramesitylporphyrins. *Inorg. Chem.* **1990**, *29* (7), 1422−1427.
(37) Messinger, J.; Robblee, J. H.; Bergmann, U.; Fernandez, C.; Glatzel, P.; Visser, H.; Cinco, R. M.; McFarlane, K. L.; Bellacchio, E.; Pizarro, S. A.; et al. Absence of Mn-centered oxidation in the S2→ S3 transition: implications for the mechanism of photosynthetic water oxidation. *J. Am. Chem. Soc.* **2001**, *123* (32), 7804−7820.
(38) Davis, K. M.; Palenik, M. C.; Yan, L.; Smith, P. F.; Seidler, G. T.; Dismukes, G. C.; Pushkar, Y. N. X-ray emission spectroscopy of Mn coordination complexes toward interpreting the electronic structure of the oxygen-evolving complex of photosystem II. *J. Phys. Chem. C* **2016**, *120* (6), 3326−3333.
(39) Pizarro, S. A.; Glatzel, P.; Visser, H.; Robblee, J. H.; Christou, G.; Bergmann, U.; Yachandra, V. K. Mn oxidation states in tri-and tetra-nuclear Mn compounds structurally relevant to photosystem II: Mn K-edge X-ray absorption and Kβ X-ray emission spectroscopy studies. *Phys. Chem. Chem. Phys.* **2004**, *6* (20), 4864−4870.
(40) Gupta, R.; Taguchi, T.; Lassalle-Kaiser, B.; Bominaar, E. L.; Yano, J.; Hendrich, M. P.; Borovik, A. High-spin Mn−oxo complexes and their relevance to the oxygen-evolving complex within photosystem II. *Proc. Nat. Acad. Sci.* **2015**, *112* (17), 5319−5324, DOI: 10.1073/pnas.1422800112.
(41) Glatzel, P.; Bergmann, U. High resolution 1s core hole X-ray spectroscopy in 3d transition metal complexes—electronic and structural information. *Coord. Chem. Rev.* **2005**, *249* (1−2), 65−95.
(42) Tsutsumi, K.; Nakamori, H.; Ichikawa, K. X-ray Mn K β emission spectra of manganese oxides and manganates. *Phys. Rev. B* **1976**, *13* (2), 929.
(43) Peng, G.; Degroot, F.; Hämäläinen, K.; Moore, J.; Wang, X.; Grush, M.; Hastings, J.; Siddons, D.; Armstrong, W. High-resolution manganese x-ray fluorescence spectroscopy. Oxidation-state and spin-state sensitivity. *J. Am. Chem. Soc.* **1994**, *116* (7), 2914−2920.
(44) Roemelt, M.; Beckwith, M. A.; Duboc, C.; Collomb, M.-N.; Neese, F.; DeBeer, S. Manganese K-edge X-ray absorption spectroscopy as a probe of the metal−ligand interactions in coordination compounds. *Inorg. Chem.* **2012**, *51* (1), 680−687.
(45) Leto, D. F.; Jackson, T. A. Mn K-edge X-ray absorption studies of oxo-and hydroxo-manganese (IV) complexes: Experimental and theoretical insights into pre-edge properties. *Inorg. Chem.* **2014**, *53* (12), 6179−6194.
(46) La Mar, G. N.; Walker, F. A. Proton nuclear magnetic resonance studies of high-spin manganese (III) complexes with synthetic porphyrins. *J. Am. Chem. Soc.* **1975**, *97* (18), 5103−5107.
(47) Stephanos, J. J.; Addison, A. W. *Electrons, Atoms, and Molecules in Inorganic Chemistry: A Worked Examples Approach*; Academic Press, 2017.
(48) Sarangi, R. X-ray absorption near-edge spectroscopy in bioinorganic chemistry: Application to M−O2 systems. *Coord. Chem. Rev.* **2013**, *257* (2), 459−472.
(49) Cho, J.; Sarangi, R.; Annaraj, J.; Kim, S. Y.; Kubo, M.; Ogura, T.; Solomon, E. I.; Nam, W. Geometric and electronic structure and reactivity of a mononuclear 'side-on'nickel (III)−peroxo complex. *Nat. Chem.* **2009**, *1* (7), 568−572.
(50) Cho, J.; Kang, H. Y.; Liu, L. V.; Sarangi, R.; Solomon, E. I.; Nam, W. Mononuclear nickel (II)-superoxo and nickel (III)-peroxo complexes bearing a common macrocyclic TMC ligand. *Chem. Sci.* **2013**, *4* (4), 1502−1508.
(51) Suga, M.; Akita, F.; Hirata, K.; Ueno, G.; Murakami, H.; Nakajima, Y.; Shimizu, T.; Yamashita, K.; Yamamoto, M.; Ago, H.; et al. Native structure of photosystem II at 1.95 Å resolution viewed by femtosecond X-ray pulses. *Nature* **2015**, *517* (7532), 99−103.
(52) Blakemore, J. D.; Crabtree, R. H.; Brudvig, G. W. Molecular catalysts for water oxidation. *Chem. Rev.* **2015**, *115* (23), 12974−13005.
(53) Zhang, B.; Sun, L. Artificial photosynthesis: opportunities and challenges of molecular catalysts. *Chem. Soc. Rev.* **2019**, *48* (7), 2216−2264.
(54) Zhang, X.-P.; Chandra, A.; Lee, Y.-M.; Cao, R.; Ray, K.; Nam, W. Transition metal-mediated O−O bond formation and activation in chemistry and biology. *Chem. Soc. Rev.* **2021**, *50* (8), 4804−4811.
(55) Davis, K. M.; Sullivan, B. T.; Palenik, M. C.; Yan, L.; Purohit, V.; Robison, G.; Kosheleva, I.; Henning, R. W.; Seidler, G. T.; Pushkar, Y. Rapid evolution of the photosystem II electronic structure during water splitting. *Phys. Rev. X* **2018**, *8* (4), 041014.
(56) Gao, Y.; Åkermark, T. r.; Liu, J.; Sun, L.; Åkermark, B. r. Nucleophilic attack of hydroxide on a MnV oxo complex: a model of the O−O bond formation in the oxygen evolving complex of photosystem II. *J. Am. Chem. Soc.* **2009**, *131* (25), 8726−8727.
(57) Kim, S. H.; Park, H.; Seo, M. S.; Kubo, M.; Ogura, T.; Klajn, J.; Gryko, D. T.; Valentine, J. S.; Nam, W. Reversible O−O bond cleavage and formation between Mn (IV)-peroxo and Mn (V)-Oxo corroles. *J. Am. Chem. Soc.* **2010**, *132* (40), 14030−14032.
(58) Li, X.; Zhang, X.-P.; Guo, M.; Lv, B.; Guo, K.; Jin, X.; Zhang, W.; Lee, Y.-M.; Fukuzumi, S.; Nam, W.; et al. Identifying intermediates in electrocatalytic water oxidation with a manganese corrole complex. *J. Am. Chem. Soc.* **2021**, *143* (36), 14613−14621.
(59) Zhang, L.; Seo, M. S.; Choi, Y.; Ezhov, R.; Maximova, O.; Malik, D. D.; Ng, M.; Lee, Y.-M.; Sarangi, R.; Pushkar, Y. N.; et al. A Manganese Compound I Model with a High Reactivity in the Oxidation of Organic Substrates and Water. *J. Am. Chem. Soc.* **2023**, *145* (15), 8319−8325.
(60) Bhowmick, A.; Hussein, R.; Bogacz, I.; Simon, P. S.; Ibrahim, M.; Chatterjee, R.; Doyle, M. D.; Cheah, M. H.; Fransson, T.;

Chernev, P.; et al. Structural evidence for intermediates during O2 formation in photosystem II. *Nature* **2023**, *617* (7961), 629−636.
(61) Moonshiram, D.; Alperovich, I.; Concepcion, J. J.; Meyer, T. J.; Pushkar, Y. Experimental demonstration of radicaloid character in a RuV= O intermediate in catalytic water oxidation. *Proc. Natl. Acad. Sci. U.S.A.* **2013**, *110* (10), 3765−3770.
(62) Alperovich, I.; Smolentsev, G.; Moonshiram, D.; Jurss, J. W.; Concepcion, J. J.; Meyer, T. J.; Soldatov, A.; Pushkar, Y. Understanding the electronic structure of 4d metal complexes: from molecular spinors to L-edge spectra of a di-Ru catalyst. *J. Am. Chem. Soc.* **2011**, *133* (39), 15786−15794.
(63) Ezhov, R.; Ravari, A. K.; Pushkar, Y. Characterization of the FeV= O complex in the pathway of water oxidation. *Angew. Chem.* **2020**, *132* (32), 13604−13607.
(64) Ezhov, R.; Ravari, A.; Bury, G.; Smith, P.; Pushkar, Y. Formation of CoIV= O intermediate at the Boundary of the "Oxo-wall" Induces Water Oxidation. *Res. Sq.* **2020**, 1−20.

https://doi.org/10.1021/acs.jpclett.4c02020
J. Phys. Chem. Lett. 2024, 15, 11077−11086